



ARTICLE

<https://doi.org/10.1038/s42003-019-0599-8>

OPEN

# 3D mapping reveals network-specific amyloid progression and subcortical susceptibility in mice

Rebecca Gail Canter<sup>1,6</sup>, Wen-Chin Huang<sup>1,6</sup>, Heejin Choi<sup>2,6</sup> , Jun Wang<sup>1</sup>, Lauren Ashley Watson<sup>1</sup>, Christine G. Yao<sup>1</sup>, Fatema Abdurrob<sup>1</sup>, Stephanie M. Bousleiman<sup>1</sup>, Jennie Z. Young<sup>1</sup>, David A. Bennett<sup>3</sup>, Ivana Delalle<sup>4\*</sup>, Kwanghun Chung<sup>1,2,5\*</sup>  & Li-Huei Tsai<sup>1\*</sup>

Alzheimer's disease (AD) is a progressive, neurodegenerative dementia with no cure. Prominent hypotheses suggest accumulation of beta-amyloid (A $\beta$ ) contributes to neurodegeneration and memory loss, however identifying brain regions with early susceptibility to A $\beta$  remains elusive. Using SWITCH to immunolabel intact brain, we created a spatiotemporal map of A $\beta$  deposition in the 5XFAD mouse. We report that subcortical memory structures show primary susceptibility to A $\beta$  and that aggregates develop in increasingly complex networks with age. The densest early A $\beta$  occurs in the mammillary body, septum, and subiculum- core regions of the Papez memory circuit. Previously, early mammillary body dysfunction in AD had not been established. We also show that A $\beta$  in the mammillary body correlates with neuronal hyper-excitability and that modulation using a pharmacogenetic approach reduces A $\beta$  deposition. Our data demonstrate large-tissue volume processing techniques can enhance biological discovery and suggest that subcortical susceptibility may underlie early brain alterations in AD.

<sup>1</sup>The Picower Institute for Learning and Memory, Department of Brain and Cognitive Sciences, Massachusetts Institute of Technology, Cambridge, MA, USA. <sup>2</sup>Institute for Medial Engineering and Science (IMES), MIT, Cambridge, MA, USA. <sup>3</sup>Rush Alzheimer's Disease Center, Rush University Medical Center, Chicago, IL, USA. <sup>4</sup>Department of Pathology and Laboratory Medicine, Boston University School of Medicine, Boston, MA, USA. <sup>5</sup>Department of Chemical Engineering, MIT, Cambridge, MA, USA. <sup>6</sup>These authors contributed equally: Rebecca Gail Canter, Wen-Chin Huang, Heejin Choi. \*email: [idelalle@bu.edu](mailto:idelalle@bu.edu); [khchung@mit.edu](mailto:khchung@mit.edu); [lhtsai@mit.edu](mailto:lhtsai@mit.edu)

Cognitive impairments attributable to Alzheimer's disease (AD) will affect millions of individuals in the next decade, however, the etiology of the disease remains largely unknown<sup>1</sup>. The results from decades of research support the hypothesis that the accumulation of toxic amyloid-beta peptides (A $\beta$ ) in the brain contributes to the onset and progression of Alzheimer's dementia<sup>2–4</sup>. The amyloid hypothesis was initially based on the discovery that mutations in the A $\beta$  precursor protein (APP) and its processing enzymes cause autosomal dominant, inherited, familial Alzheimer's dementia (FAD)<sup>5</sup>. Subsequent preclinical studies demonstrating that A $\beta$  peptides induce synaptic loss and neuronal death in vitro and in vivo have further established that A $\beta$  is acutely toxic to the neural substrate. In addition to cellular harm, amyloidosis in murine models of AD contributes to AD-like memory impairments, hippocampal synaptic loss, and electrophysiological alterations—changes that are also observed in human patients with amyloid<sup>6–8</sup>. Together, the preclinical and genetic data suggest that A $\beta$  directly impacts the neurodegeneration that is observed FAD<sup>9–11</sup> and also provide a basis for understanding the etiology of the sporadic form of the disease. Despite the link between A $\beta$  toxicity and neurodegeneration in multiple forms of AD, the precipitating events that trigger A $\beta$  accumulation, deposition, and progression remain unclear.

One impediment to understanding the relationship between A $\beta$  deposition and the onset of AD has been identifying the brain regions that are most vulnerable to A $\beta$  plaques. The first studies using postmortem brain sections from AD patients' brains suggested that initial accumulation of A $\beta$  occurs in the neocortex with subsequent spread of aggregates to deeper structures implicated in learning and memory<sup>12</sup>. However, due to the use of postmortem specimens, these reports could not document A $\beta$  deposition over time prior to the development of AD dementia. Recent advances in positron emission tomography (PET) imaging have enabled longitudinal human A $\beta$ -imaging studies that confirm the importance of cortical A $\beta$  in the diagnosis and prediction of progression of cognitive impairment<sup>13,14</sup>, although they have largely not examined deeper structures for A $\beta$  load and spread<sup>14,15</sup>. Intriguingly, while cortical A $\beta$  correlates with dementia status in patients<sup>16,17</sup>, many cognitively healthy individuals also have high levels of cortical A $\beta$ <sup>18</sup>. A recent paper using PET staging showed a pattern of A $\beta$  progression that was constant across individuals, regardless of clinical diagnosis, consistent with previous postmortem studies<sup>19</sup>. In addition, patients diagnosed with non-Alzheimer's dementia-related neurodegenerative diseases, like Parkinson's, showed regional A $\beta$  vulnerability that correlates with cognitive and motor impairments<sup>20</sup>. This discrepancy between cortical accumulation and cognitive impairment suggests that a systematic and comprehensive approach to studying A $\beta$  deposition may reveal unexplored A $\beta$ -related changes in the brain that contribute proximally to memory-related alterations in Alzheimer's dementia<sup>21</sup>.

Increasing evidence suggests that A $\beta$  affects distributed memory networks in AD and that dysfunction in one or more of these networks may underlie cognitive decline. However, there are inconsistencies in these observations. Neuroimaging studies have revealed structural and functional alterations in high-level cortical networks like the default-mode network (DMN)<sup>15,22</sup>, while other recent findings show core alterations in fundamental deep memory structures that are part of the limbic system<sup>8,23–25</sup>. Although the networks underlying memory and those implicated by neuroimaging studies somewhat overlap, there are distinct brain areas and functions that the networks do not share. Because of this discrepancy, it remains uncertain where the most critical early network alterations occur in AD. Furthermore, the question of whether subcortical areas show differential susceptibility to

cortical regions remains unexplored in most human neuroimaging studies.

One aspect that likely contributes to the difficulty discerning network alterations in AD is the challenge of staging patient disease progression. The complexity arises from the number of disease components that affect cognitive status, including variable pathological loads across patients<sup>21</sup>, as well as the socioeconomic, lifestyle, and genetic factors that influence AD<sup>26</sup>. To overcome the inherent variability in and technical limitations of studying human disease, in this work we started by capitalizing on the temporal precision of murine models to map A $\beta$  progression at high-resolution throughout the brain of transgenic 5XFAD mice, which harbor five familial AD mutations—three in human APP and two in human PSEN1<sup>27,28</sup>. We use optimized techniques for whole-brain System-Wide Control of Interaction Time and kinetics of Chemicals (SWITCH) immunolabeling<sup>29</sup> to create the unbiased and comprehensive map of A $\beta$  deposition at high spatial and temporal resolution. Our observations reveal subcortical susceptibility to A $\beta$  deposition in several regions of the Papez circuit, such as the dorsal subiculum, septum, and mammillary body. While other studies have implicated the subiculum in early AD, we were surprised to learn that the mammillary body, an area important in anterograde memory and spatial navigation, also may be vulnerable. We show that the MB neurons undergo functional alterations concurrent with early aggregate development and that modulating neural activity to counteract the functional changes, we observed lessens the A $\beta$  burden in the mouse model. Together, our data suggest that the MB, as part of the Papez circuit, is a relevant and susceptible subcortical hub in the development of AD.

## Results

**Optimized SWITCH enables whole-brain immunolabeling.** For a comprehensive and spatially unbiased, temporally precise map of amyloidosis in a murine model of AD, we needed to label intact tissue specimens that we could image at a cellular scale. This would enable us to create a specific pathological map like with traditional histology, but without the loss of critical information to the size limitations and directional segmentations that are inherent in tissue-sectioning studies. We chose to use SWITCH techniques because they enable homogenous, whole-brain immunolabeling using readily accessible laboratory reagents<sup>29</sup>. Although the SWITCH techniques are widely applicable to many antibodies and target proteins<sup>29</sup>, we discovered that we needed to further refine the buffer systems to achieve homogenous whole-brain labeling with our chosen antibodies. In our optimized SWITCH system (Fig. 1a), we modulate the pH and ionic strength of the buffers to control antibody-antigen binding kinetics<sup>30</sup>. In the first step of our new protocol, we use a high-pH and high ionic-strength buffer to slow the binding reaction. This modulation allows antibodies to penetrate deep into the sample passively, regardless of the antigenic content in the tissue. In the second step, we titrate the buffer back to a physiological pH and ionic strength to re-enable antibody binding. By employing this system, we achieved homogenous labeling throughout thick tissue sections using an antibody to myelin basic protein (MBP), an extremely abundant antigen (Supplementary Fig. 1A). In addition, we reduced signal intensity changes through the thickness of the tissue (Supplementary Fig. 1B) and created a signal attenuation profile consistent with light loss through the sample, rather than due to non-homogenous labeling within the specimen (Supplementary Fig. 1C).

Despite showing the protocol worked with MBP antibodies in thick tissue sections, we needed to ensure that our optimized



**Fig. 1** SWITCH labeling reveals Papez circuit vulnerability and network propagation of amyloid pathology. **a** Schematic of the System-Wide Control of Interaction Time and kinetics of Chemicals (SWITCH) protocol. **b** Representative images of amyloid labeling in a brain from a 12-month-old mouse. Whole hemisphere 2D images of the 3D-rendered brain from the medial and lateral view. Additional representative optical sections showing the sagittal distribution, horizontal distribution, and three coronal sections. Scale bars 1000  $\mu\text{m}$ . **c** Amyloid density plot of average amyloid density for each age time point.  $N = 2$  or 3/group. Log<sub>2</sub>-transformed deposit count/mm<sup>3</sup> of tissue. The data plotted in rank-order of 12-month animal density. Six-, 4-, and 2-month data overlaid on top of 12 M data for comparison.  $N = 1$  (4 M);  $N = 2$  (2 M, 6 M),  $N = 3$  (12 M) independent biological samples. **d–g** Representative images of amyloid labeling in brains from **(d)** 6-, **(e)** 4-, **(f)** 2-, **(g)** 1-month-old mice. Scale bars 500  $\mu\text{m}$ . **d** There is significant amyloid deposition in cortex, as well as aggregates in the hippocampus, amygdala, and other limbic structures in 6-month-old brains. **e** Representative images from 4-month-old brains show significant accumulation in the default-mode-related frontal cortex, and regions that are part of the Papez circuit (e.g., septum, subiculum, mammillary body). **f** Optical sections from 2-month-old brains showing sparse amyloid labeling, except for accumulation in the mammillary body, septum, and subiculum. **g** In 1-month-old brains, only a few small deposits can be seen in the subiculum and mammillary body. **h** Hierarchical clustering of log<sub>2</sub>-transformed average density data by region. Euclidean distance, average linkage. Scale bar is not symmetric around 0. Optimal leaf order enabled, which plots most similar groups nearest each other in the graph. Colored branches represent groups labeled on right y-axis

in addition to the previously reported cortical and hippocampal regions (Supplementary Fig. 1D–F). These proof-of-concept samples confirmed that our SWITCH-based large tissue volume technique was a reliable tool to analyze intact specimens and suggested that we might be able to uncover interesting biology by using the new technique to investigate regional amyloid burden<sup>32</sup>.

**Spatiotemporal analyses reveal papez circuit vulnerability.** To quantify regional burden more comprehensively and at a higher spatial resolution, especially in the interesting subcortical areas, we carried out the SWITCH procedure on brains from a cohort of 12-month (12 M)-old 5XFAD mice (Fig. 1b; Supplementary Movie 2D). Region-specific quantification from white matter-based hand annotation of three-dimensional (3D) images showed substantial A $\beta$  deposition throughout the brains and confirmed accumulation in AD-associated areas (Fig. 1c). The regions harboring A $\beta$  included the retrosplenial cortex (RSP), hippocampus (HPC), subiculum (SUB), and anterior cingulate cortex (ACC), and prefrontal cortex (PFC). Importantly, deposits were largely absent from areas that appear less vulnerable to A $\beta$  aggregation in human AD brains, such as the caudoputamen (CP) and globus pallidus (GP). Differences in A $\beta$  levels across regions were significant (D’Agostino and Pearson normality test;  $K_2 = 94.61$ ,  $p < 0.0001$ , passed normality = no; Friedman test;  $Q = 114.2$ ,  $p < 0.0001$ ), which suggests that the peptide accumulates within particular brain areas and does not deposit unvaryingly across the brain. Unexpectedly, the highest aggregate density by rank in the 12 M animals appeared within specific subcortical regions, namely the medial nucleus of the mammillary body (MB) and septum (SEPT).

The regional differences in A $\beta$  and unexpected high density in small subcortical nuclei might develop because aggregates in the 5XFAD animals arise uniformly throughout the brain over time, thus making these smaller structures appear denser. Alternatively, the high-density regions could show unique vulnerability to form aggregates in conditions of elevated A $\beta$ , leading to earlier or more substantial deposition. To observe which model better explains the amyloid distribution, we applied our optimized SWITCH protocol to map the sequence of amyloid deposition back to the earliest time points by analyzing brains from 6, 4, 2, and 1-month (6 M, 4 M, 2 M, 1 M, respectively)-old 5XFAD mice (Supplementary Movie 2A–C). We quantified A $\beta$  density in many regions across multiple animals at each time point in a similar manner as in the 12 M brains, and observed increasingly specific aggregation with decreasing age in a pattern that was consistent across individuals. At 6 M, 5XFAD brains displayed region-specific aggregation (Fig. 1d), with areas harboring significantly different densities of amyloid (Fig. 1c; D’Agostino and Pearson normality test;  $K_2 = 70.12$ ,  $p < 0.0001$ , passed normality = no; Friedman test;  $Q = 68.56$ ,  $p = 0.0171$ ). To better understand the brain areas

that contribute to region-specific aggregation in our data, we performed hierarchical clustering analysis on the log<sub>2</sub> transform of the regional data averages from each age cohort (Fig. 1h, Euclidean distance, average linkage). The clustering revealed a number of groups, each of which contained areas that function as nodes in specific cognitive networks (Table 1). At 6 M, the hippocampus, olfactory, and corticolimbic (e.g., basolateral amygdalar complex (BLA), piriform cortex (PIR), entorhinal cortex (EC)) systems first show appreciable levels of A $\beta$  (Table 2). This result was particularly interesting because the clustering analysis is based solely on aggregate numbers and it found that the density of A $\beta$  is relatively uniform within functional networks, and also unbiasedly identified circuits that underlie behaviors and cognitive functions known to show alterations in early Alzheimer’s dementia<sup>33</sup>.

To further refine our understanding of the sequence of A $\beta$  deposition, we next looked at 4 M-aged brains in the 5XFAD predictable, genetic murine model (Fig. 1e). Importantly, at 4 M, the data continue to demonstrate an increasingly precise, area-specific aggregation which our analyses confirmed as a non-normal, nonlinear pattern to the regional distribution (Fig. 1c; D’Agostino and Pearson normality test;  $K_2 = 51.67$ ,  $p < 0.0001$ , passed normality = no; nonlinear Regression;  $y = -354.1 \cdot \ln(x) + 1200.9$ ,  $R^2 = 0.82465$ ). The skewed data suggest that fewer brain regions have high burden, consistent with increasingly specific patterns of aggregation at the earliest stages of amyloidosis. To determine which regions have aggregates at 4 M, we looked at our clustering analyses (Fig. 1h) which revealed that regions homologous to the those in the DMN (e.g., retrosplenial (RSP), anterior cingulate (ACC), and parietal cortices)<sup>34</sup> are better correlated to each other (Table 1) and first show A $\beta$  in 4 M brains (Table 2). At 4 M, there was no appreciable A $\beta$  in olfactory or extended limbic areas (Fig. 1h).

Human functional studies have suggested that the DMN is the earliest affected functional network<sup>35,36</sup>. Thus, to determine if our murine amyloid model reflected this human finding, we next looked at 2 M brains to understand whether there are earlier affected areas. At 2 M, there were very few brain regions with observable A $\beta$  (Fig. 1f), and the brains failed to demonstrate significant differences across areas (Fig. 1c; D’Agostino and Pearson normality test;  $K_2 = 105.2$ ,  $p < 0.0001$ , passed normality = no; Friedman test;  $Q = 58.18$ ,  $p = 0.1073$ ). The unbiased clustering revealed that at 2 M, A $\beta$  deposition is similar across most of the brain, confirming our density observations (Fig. 1h). However, the clustering analysis also indicated a few specific areas with distinct and correlated deposition in the 2 M animals (Table 2). These key nodes of early aggregation were the MB, SEPT, and SUB—regions that connect the HPC to the rest of the Papez memory circuit<sup>37</sup>. At 1 M, animals did not show discernable A $\beta$  accumulation anywhere, except for a few small

**Table 1 Regional group assignments from Fig. 1**

Group	Regions	Primary network	Secondary networks
-	MB	Papez	
1	vSub, dSub, LS, RSP, ACC, MC	Papez	Default mode
2	MS, DB	Cholinergic	
3	BLA, Thal, OT, MOB	Limbic	Olfactory
4	EC, ACB, MD, SS, DP, TT, AON	Cortex	Olfactory, basal ganglia
5	PFC, OFC, PTL, IC, VIS, TR	Cortex	
6	dDG, dCA1, vDG, vCA1, vCA3, Peri, AUD, TEA, Pir, GC, Visc	Hippocampus	Cortex
7	dCA3, CeA, SI, PAA, COA, BNST, HYP, CP	Limbic	Straitum
-	GP	Striatum	

ACC anterior cingulate cortex, RSP retrosplenial cortex, vSub ventral subiculum, LS lateral septum, dSub dorsal subiculum, MC motor cortex, DB diagonal band, MS medial septum, ACB nucleus accumbens, PIR piriform cortex, MD midbrain, Thal thalamus, BLA basolateral amygdala, OT olfactory tubercle, PERI perirhinal and entorhinal cortices, GC gustatory cortex, IC insular cortex, VIS visual cortex, PTL posterial parietal association areas, SS somatosensory cortex, DP dorsal peduncular area, AON anterior olfactory nucleus, EC entorhinal cortex, PFC prefrontal cortex, OFC orbitofrontal cortex, TR postpiriform transition area, TT tenia tecta, dDG dorsal dentate gyrus, Visc visceral cortex, TEA temporal association areas, AUD auditory cortex, dCA1 dorsal CA1, vDG ventral dentate gyrus, vCA1 ventral CA1, vCA3 ventral CA3, dCA3 dorsal CA3, CP caudoputamen, BNST bed nucleus of the stria terminalis, HYP hypothalamus, CeA centromedial amygdalar nuclei, SI substantia innominata, PAA piriform amygdalar area, COA cortical amygdalar area

Primary and secondary network assignment based on the regions in the group and major networks that appear in literature searches associated with each region

**Table 2 Group-network data summarized from Fig. 1**

Network	Groups	Age of A $\beta$ appearance
Papez	MB, 1, 3	2 months
Cholinergic	1, 2	2 months
Default mode	1, 4	4 months
Sensorimotor cortex	1, 5, 6	4 months
Olfactory	3, 4, 6	6 months
Extended limbic	3, 4, 5, 7	6 months
Hippocampus	6, 7	6 months
Striatum	7, GP	12 months

ACC anterior cingulate cortex, RSP retrosplenial cortex, vSub ventral subiculum, LS lateral septum, dSub dorsal subiculum, MC motor cortex, DB diagonal band, MS medial septum, ACB nucleus accumbens, PIR piriform cortex, MD midbrain, Thal thalamus, BLA basolateral amygdala, OT olfactory tubercle, PERI perirhinal and entorhinal cortices, GC gustatory cortex, IC insular cortex, VIS visual cortex, PTL posterial parietal association areas, SS somatosensory cortex, DP dorsal peduncular area, AON anterior olfactory nucleus, EC entorhinal cortex, PFC prefrontal cortex, OFC orbitofrontal cortex, TR postpiriform transition area, TT tenia tecta, dDG dorsal dentate gyrus, Visc visceral cortex, TEA temporal association areas, AUD auditory cortex, dCA1 dorsal CA1, vDG ventral dentate gyrus, vCA1 ventral CA1, vCA3 ventral CA3, dCA3 dorsal CA3, CP caudoputamen, BNST bed nucleus of the stria terminalis, HYP hypothalamus, CeA centromedial amygdalar nuclei, SI substantia innominata, PAA piriform amygdalar area, COA cortical amygdalar area

Ordered by group average (MB-0, GP-8). Age of appearance assigned based on log-scale values for majority of regions > 4

deposits in the MB (Fig. 1g), and these results are consistent with previous reports<sup>28</sup> that deposition is largely not developmental. Overall, the spatiotemporal map supports a model where the SUB, MB, and SEPT are uniquely susceptible to A $\beta$  aggregation and show the densest A $\beta$  because they accumulate pathology over a longer period. This suggests that, over time, regional A $\beta$  burden progresses to include more areas and that accumulation within a brain region may be dependent on factors that confer differential propensities to develop aggregates.

To ascertain whether the subcortical aggregation pattern is an artifact of the mouse transgene, we performed dual immunofluorescence for A $\beta$  aggregates and in situ hybridization for the transgenic mRNA, so we could correlate the location of A $\beta$  deposits with expression patterns of the transgene (Fig. 2a). We expected the transgene expression to remain stable across differently aged brains and, in our analyses, patterns of transgene expression in both 2 M and 4 M animals looked comparable across the subregions we analyzed. The correlation analyses between transgenic mRNA and A $\beta$  deposits at the early time points demonstrates that across the entire brain, transgenic RNA expression does not correlate with deposit location, and many

brain areas that have high transgene expression do not have plaques, even up to 4 M-old brain (Fig. 2b; Spearman correlation  $r = -0.0728$ ,  $p = 0.3616$ ). The results remained nonsignificant when we carried out the analysis splitting the data by brain region (Fig. 2c). The lack of correlation between A $\beta$  aggregates and APP mRNA suggests that plaque burden in the 5XFAD animals is not exclusively dependent on the levels of transgene expression and that the brains show biologically relevant, region-specific amyloid deposition.

Together the spatiotemporal map in mice and biological relevance of region-specific deposition show that the core regions connecting the HPC to the rest of the Papez circuit—the MB, SEPT, and SUB—are particularly prone to A $\beta$  deposition. Then, over time, the aggregates appear in increasingly complex cognitive systems moving next to the DMN, followed by the extended limbic system, before finally developing throughout the entire forebrain. Importantly, looking at human MB using SWITCH (Supplementary Movie 3; subject information in Supplementary Table 1) or immunofluorescent labeling (Supplementary Fig. 2A; subject information in Supplementary Table 2) demonstrates A $\beta$  deposition is significantly higher in individuals with a clinical diagnosis of AD (Supplementary Fig. 2B, Shapiro–Wilk normality test, healthy:  $W = 0.7735$ ,  $p = 0.0069$ , passed normality = no, AD:  $W = 0.9129$ ,  $p = 0.4561$ , passed normality = yes; Kolmogorov–Smirnov test,  $D = 0.6667$ ,  $p = 0.0420$ ) and that higher percent MB area with A $\beta$  correlated with increased likelihood of pathological diagnosis of AD (Supplementary Fig. 2C, Spearman correlation, CERAD: Spearman  $r = -0.4142$ ,  $p = 0.1115$ , Braak:  $r = 0.5774$ ,  $p = 0.0210$ , NIA–Reagan:  $r = -0.5086$ ,  $p = 0.0459$ ). This suggests that human brain alterations in AD look similar to what we observe in mouse. Thus we propose that A $\beta$  deposits start in susceptible subcortical structures and spread to increasingly complex memory and cognitive networks with age.

**Papez structures are susceptible to dysfunction.** A prevailing hypothesis is that A $\beta$ -induced electrophysiological dysfunction underlies cognitive decline and studies have shown that hyperexcitability—like that seen in AD patients—can increase the deposition of A $\beta$ . Thus, we set out to determine whether alterations in neuronal activity like those in the cortex and hippocampus may also be a factor that contributes to regional vulnerability in the subcortical structures we identified<sup>7,25,38,39</sup>. In our spatiotemporal map data, we found that the MB showed the densest A $\beta$  at the earliest stages. This region plays a key role in

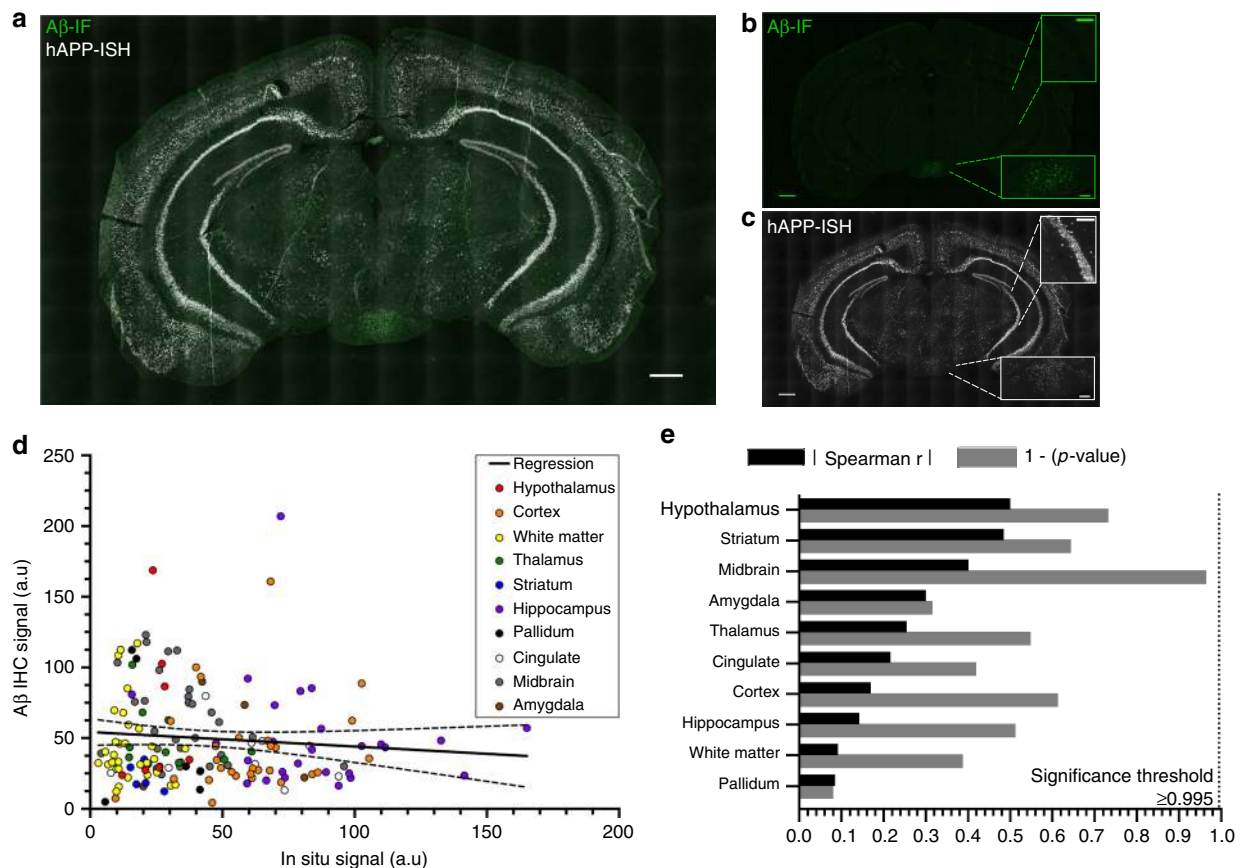
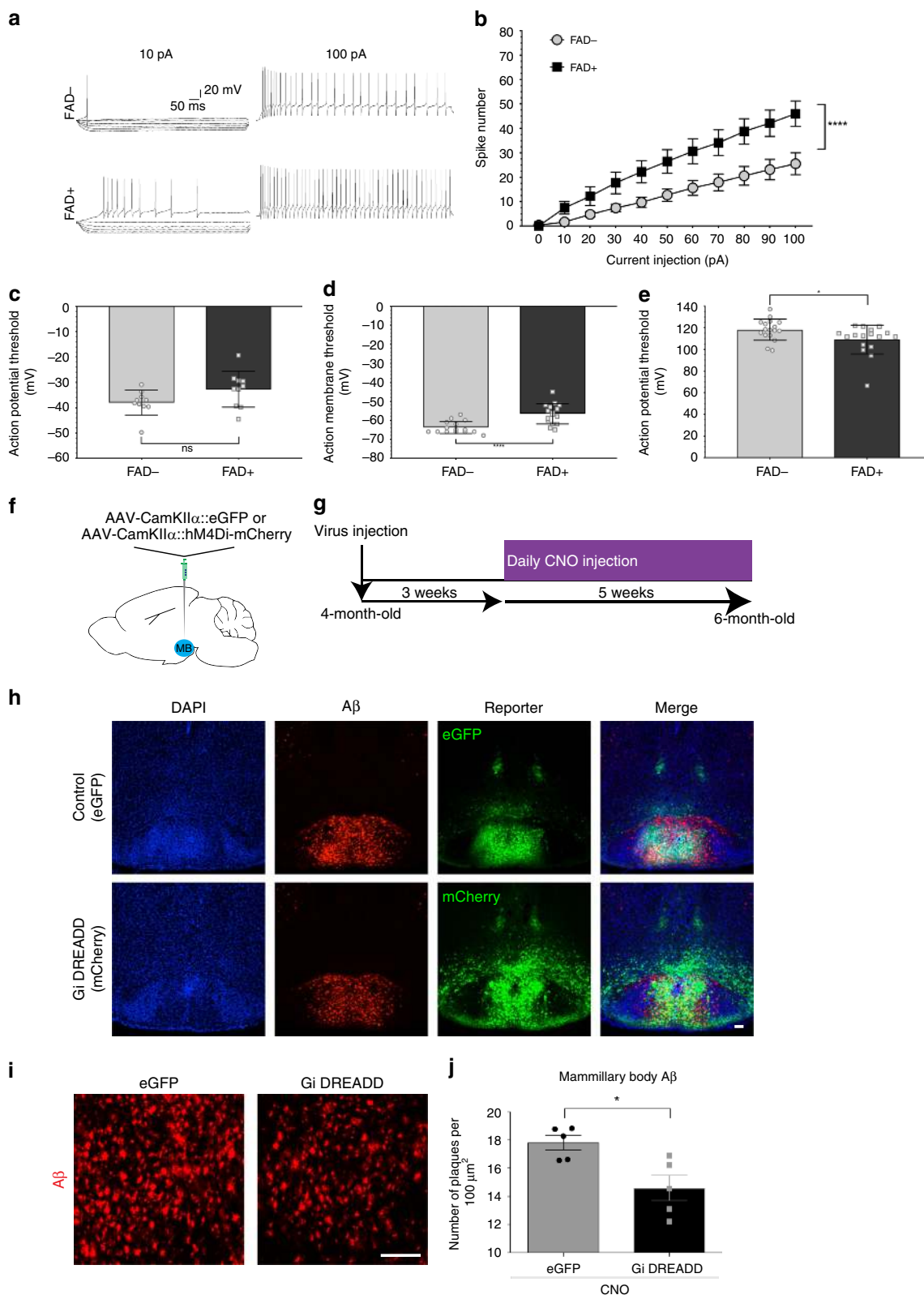


**Fig. 2** Progression patterns cannot be described by transgenic mRNA expression. **a** Representative merged image of amyloid immunofluorescent labeling (green) and APP mRNA in situ hybridization (white). Scale bar 500  $\mu\text{m}$ . **b** Unmerged image of amyloid immunofluorescence signal. Scale bar 500  $\mu\text{m}$ . Insets show mammillary body area with significant A $\beta$  accumulation and hippocampus with very little A $\beta$  accumulation. Inset scale bars 150  $\mu\text{m}$ . **c** Unmerged image of APP in situ hybridization. Scale bar 500  $\mu\text{m}$ . Mammillary body area shows lower hAPP mRNA expression than the hippocampus. Inset scale bars 150  $\mu\text{m}$ . **d** Correlation between amyloid-IF signal and APP in situ. Colored dots represent separately quantified regions. Linear regression and correlation analyses carried out on the combined data. Linear regression:  $Y = -0.1027x + 54.28$ ;  $F_{(1,157)} = 1.333$ ,  $p = 0.2501$ . No significant deviation from zero. Spearman  $r = -0.07284$ ;  $p = 0.3616$ . **e** Spearman correlation for in situ hybridization-immunofluorescence data by region. Black bars represent Spearman rho, gray bar represents  $1 - p$ -value of Spearman correlation. Significance threshold  $\alpha = 0.05$  with Bonferonni correction for ten regions

spatial and anterograde memory in mice and humans<sup>40–42</sup>, and these two aspects of cognitive function decline in AD. Thus, we wanted to determine whether the A $\beta$  accumulation we observed in the MB was associated with any functional changes that may confer susceptibility. We performed ex vivo whole-cell patch-clamp recordings in MB in slices from 5XFAD mice and littermate controls. Even at 2 M, we found that 5XFAD MB neurons showed significantly higher intrinsic excitability (Fig. 3a), with a significantly larger number of action potentials elicited by incremental depolarizing current steps (Fig. 3b, two-way repeated measures ANOVA; interaction:  $F_{(10,310)} = 6.855$ ,  $p < 0.0001$ ; genotype:  $F_{(1,31)} = 7.166$ ,  $p = 0.0118$ ). Although the threshold for action potentials in MB neurons did not differ between groups (Fig. 3c, unpaired Student's  $t$  test;  $t_{(18)} = 1.924$ ,  $p = 0.0704$ ), the resting membrane potential differed significantly from WT controls and was on average  $\sim 7.3$  mV more depolarized in MB neurons from 2 M 5XFAD mice (Fig. 3d; unpaired Student's  $t$  test;  $t_{(29)} = 4.509$ ,  $p < 0.0001$ ). Finally, we also observed a slightly increased action potential amplitude in 2 M 5XFAD mice (Fig. 3e; D'Agostino and Pearson normality test, FAD $^-$ :  $K2 = 0.6008$ ,  $p = 0.7405$ , passed normality = yes; FAD $^+$ :  $K2 = 20.61$ ,  $p < 0.0001$ , passed normality = no; Mann-Whitney  $U$ ;  $U = 77$ ,  $p = 0.0196$ ), which likely also contributes to the overall observed hyperexcitability. This observation suggests that high levels of A $\beta$  contribute to dysfunction, even in deep, subcortical structures.

**Modulating activity in the MB reduces A $\beta$  pathology.** Studies have reported that neuronal activity can regulate A $\beta$  production and deposition such that inducing neuronal activity increases A $\beta$  levels and inhibiting activity reduces it<sup>43–46</sup>. To test whether the hyperexcitability we observed in the MB affects A $\beta$  deposition in 5XFAD mice, we modulated neuronal activity in MB excitatory neurons using an inhibitory Designer Receptor Exclusively Activated by Designer Drug (DREADD)<sup>47</sup>. We stereotactically injected either AAV-CamKII $\alpha$ -eGFP (eGFP) or AAV-CamKII $\alpha$ -hM4Di-mCherry (Gi DREADD) into MB of 4-month-old 5XFAD mice (Fig. 3f). We allowed for 3 weeks of postoperative recovery and time for expression of viral vectors and then gave daily intraperitoneal (IP) injections of clozapine-N-oxide (CNO) to activate the inhibitory DREADD receptors to reduce MB activity over a period of 5 weeks (Fig. 3g). We confirmed the expression of eGFP or hM4Di-mCherry in MB (Fig. 3h) and analyzed whether prolonged reduction of MB activity affected the amount of A $\beta$  in the region (Fig. 3i). We saw a significant reduction in MB A $\beta$  in the Gi DREADD-expressing group compared with eGFP controls (Fig. 3j, Unpaired Student's  $t$  test;  $t_{(8)} = 3.137$ ,  $p = 0.0139$ .  $*p < 0.05$ ). Because regulation of MB activity affected A $\beta$  deposition, this finding indicates that the hyperexcitability we observed in MB neurons may contribute to the worsening A $\beta$  load in the region over time. In addition, because we intervened at an advanced stage of amyloidosis, our



data also suggest that regulating activity can slow pathological progression later in the disease.

To understand whether chronically inhibiting activity in the MB also led to changes of Aβ deposition in the interconnected brain regions, we further measured the amount of Aβ plaque in the dorsal subiculum, an upstream brain region that project to the MB, and the anterior thalamus, a brain region downstream from

the MB<sup>42</sup>. We found that prolonged inhibition of the MB does not significantly alter Aβ in the dorsal subiculum (dSUB) (Supplementary Fig. 3A, unpaired Student's *t* test;  $t_{(8)} = 1.173$ ,  $p = 0.2745$ ), suggesting that manipulating activity does not affect Aβ deposition in the upstream brain region. We then tried to quantify Aβ deposition in the anterior thalamus downstream of the MB. In doing so, we observed too little Aβ to compare

**Fig. 3** MB shows significant functional alterations in young 5XFAD mice. **a** Representative traces of neuronal patch-clamp recordings from mammillary body slices from 5XFAD + (FAD +) and 5 × FAD- (FAD-) at 10 pA and 100 pA. **b** Excitability curve showing the spike number from 5XFAD + and 5XFAD- mammillary body neurons at each current injection step from 0 to 100 pA. Repeated measures ANOVA. Genotype:  $F_{(1,31)} = 7.166$ ,  $p = 0.0118$ ; current injection:  $F_{(10,310)} = 94.22$ ,  $p < 0.0001$ ; interaction:  $F_{(10,310)} = 6.855$ ,  $p < 0.0001$ .  $N = 17$  cells/group. Graph reports mean  $\pm$  standard error. **c** Action potential threshold in mammillary body neurons is not significantly different between 5XFAD + and 5XFAD-. Unpaired Student's  $t$  test;  $t_{(18)} = 1.924$ ,  $p = 0.0704$ . Each dot represents a single cell. Graph reports group mean  $\pm$  standard deviation. **d** Resting membrane potential is significantly depolarized in 5XFAD mammillary body neurons compared with 5XFAD-. Difference between means = 7.24 mV. Unpaired Student's  $t$  test;  $t_{(29)} = 4.509$ ,  $p < 0.0001$ . Each dot represents a single cell. Graph reports group mean  $\pm$  standard deviation. **e** Action potential amplitude is significantly decreased in 5XFAD + mammillary body neurons compared with 5XFAD-. D'Agostino and Pearson normality test, FAD-:  $K2 = 0.6008$ ,  $p = 0.7405$ , passed normality = yes; FAD +:  $K2 = 20.61$ ,  $p < 0.0001$ , passed normality = no; Mann-Whitney  $U$ ;  $U = 77$ ,  $p = 0.0196$ . Each dot represents a single cell. Graph reports group mean  $\pm$  standard deviation. **f** Cartoon illustrating the injection of AAV-CamKII $\alpha$ ::eGFP or AAV-CamKII $\alpha$ ::hM4Di-mCherry (Gi DREADD). **g** Diagram illustrating the time course of virus and CNO injections in the 5XFAD mice. **h** Images of the mammillary body in AAV-CamKII $\alpha$ -EGFP or AAV-CamKII $\alpha$ -hM4Di-mCherry (Gi DREADD) injected 5XFAD mice. DAPI (blue), A $\beta$  (red), and reporter (green: EGFP or mCherry). Scale bar 100  $\mu$ m. **i–j** Images (**i**) and quantification (**j**) of A $\beta$  plaque (red) in the mammillary body of control and Gi DREADD mice. Scale bar 100  $\mu$ m. Unpaired Student's  $t$  test;  $t_{(8)} = 3.137$ ,  $p = 0.0139$ . \* $p < 0.05$ .  $N = 5$  mice per group. Graph reports mean  $\pm$  standard error

between the control and Gi DREADD groups (Supplementary Fig. 3B). Although the anterior thalamus is the primary output of the MB, we also noticed eGFP- and mCherry-labeled axons in the dentate gyrus (DG) (Supplementary Fig. 3C). Upon further investigation, we observed expression of eGFP and Gi DREADD in the supramammillary body (SUM), a brain region immediately adjacent to the top of the MB (Fig. 3h) that projects to the DG. Because we observed this in the majority of animals we used in the studies, we concluded that our injection technique did not allow us to restrict AAV to the MB without also introducing virus into the SUM.

We decided to use the presence of eGFP or Gi DREADD in the SUM to understand how manipulating activity affects A $\beta$  in downstream regions, because we were unable to do so from the MB. To do this, we analyzed A $\beta$  deposition in the DG following our prolonged inhibition paradigm. We observed a reduction of A $\beta$  plaque in the DG after prolonged inhibition of activity in the SUM (Supplementary Fig. 3C, unpaired Student's  $t$  test;  $t_{(8)} = 2.653$ ,  $p = 0.0291$ . \* $p < 0.05$ ). Although little A $\beta$  plaque is observed in the SUM at this age, this result importantly indicates that chronically inhibiting activity in one brain region can lead to a reduction of A $\beta$  plaque in the downstream brain region.

## Discussion

Using optimized SWITCH whole-brain clearing and immunolabeling technologies, we created a spatially unbiased map of the progression of A $\beta$  deposits that revealed area-specific aggregation over time and revealed novel subcortical hubs of early-disease susceptibility in the 5XFAD mouse model of AD. We showed that the initial accumulation of A $\beta$  correlates with electrophysiological changes, which then confer additional susceptibility to accumulating pathology. Our data suggest that subcortical memory network hubs may be critically susceptible to pathological changes that occur in AD and that alterations within them may contribute to memory loss in Alzheimer's dementia.

Papez circuit dysfunction is a prevailing theory of memory loss in AD. Although the MB is a critical part of the Papez long-term memory circuit connecting the hippocampus to the anterior thalamus<sup>37</sup>, it has not been strongly implicated in Alzheimer's dementia<sup>37,48–51</sup>. This is somewhat surprising because its major inputs, the subiculum and prefrontal cortex<sup>52</sup>, have been shown to demonstrate substantial synaptic loss that correlates with memory performance<sup>53–56</sup>. In addition, the septum, which is another core node in the Papez circuit, was initially implicated in early AD by the cholinergic hypothesis. This idea posited that loss of neurons in the septum and other cholinergic nuclei were causative in disease onset and progression<sup>57</sup>. Although the idea was overshadowed by the amyloid cascade hypothesis<sup>2</sup>,

integrating our findings with the data on the hippocampus, subiculum, and septum, there is now strong evidence that each of the nodes in the Papez circuit is particularly vulnerable early in AD. Our data, along with other recent evidence for Papez circuit dysfunction<sup>58,59</sup>, suggest that not only do these subcortical structures develop A $\beta$  deposits early in AD but that they also demonstrate neural activity changes, cellular and synaptic loss, and pathological tau aggregation that may contribute to circuit-wide deficits that likely affect cognition<sup>60</sup>. Although previous studies have focused on different types of A $\beta$  or shown correlational relationships between regions, the data in this paper strengthen the evidence for dysfunctional memory circuits as a core pathology underlying AD both by revealing Papez-wide susceptibility to A $\beta$  deposition using novel techniques and by demonstrating functional consequences and pathological implications of A $\beta$  in an underexplored node in the circuit<sup>7,25,39,61</sup>.

In addition to enhancing our understanding of the regions and circuits that show primary A $\beta$  aggregation and that undergo early functional destabilization, our data suggest A $\beta$  propagates between connected brain regions by showing the affliction of increasingly complex yet interconnected memory networks with age<sup>62</sup>. This provides a unifying view of early lesions that were previously at odds between pathological and neuroimaging data, creating a framework in which to better interpret human pathogenesis. Investigators have suggested that the DMN, limbic system, attentional systems, and brain stem may all be involved at the earliest stages of prodromal AD. The data presented in this paper suggest that these do not need to be disparate hypotheses, but instead represent different stages of network affliction that occur as the disease progresses. In the mouse model, 2 M 5XFAD animals show core limbic affliction, followed by the DMN at 4 M and typical limbic system at 6 M. These observations suggest that early AD may be best staged by the network aberrations detected by functional MRI techniques. These alterations occur before overt memory loss<sup>36</sup>, and with increasing evidence for restoration of network function as a successful treatment in AD models<sup>7,63,64</sup>, our data may lay the ground work for network-progression staging to guide early-disease circuit interventions.

In humans with Alzheimer's dementia, a slow accumulation of altered cellular processes, including A $\beta$  deposition, and disrupted neural circuits long precedes cognitive deficits, such that clinical diagnosis often does not happen until much later in the progression of AD<sup>27,65</sup>. In this study, we demonstrate a similar propensity for early A $\beta$  accumulation and altered electrophysiological function as early as 2 M in the 5XFAD model, with a delay in behavioral impairments until ~6 M of age. We utilized a chemogenetic approach to reduce MB activity in this key node of the Papez circuit, and found a significant reduction in MB A $\beta$



levels. Importantly, we did not manipulate activity levels until animals were almost 5-month-old, when A $\beta$  pathology has already spread to additional brain regions and networks. This suggests that interventions within key nodes may have the potential to impact pathology, and that it may be possible to alter cognitive outcomes with this type of strategy even near the projected onset of cognitive decline. Because the regions in the basal forebrain are linked in our data, and other studies, to the hypothalamic diencephalic limbic structures, we suggest in-depth examinations of these regions and their connections may lead to a better understanding of the mechanisms of dysfunction underlying AD onset and the ensuing progressive memory loss.

## Methods

**Animals.** All mouse work was approved by the Committee for Animal Care of the Division of Comparative Medicine at the Massachusetts Institute of Technology. 5XFAD (Tg 6799) breeding pairs were acquired from the Mutant Mouse Resource and Research Center (MMRRC) (Stock No. 034848-JAX) and maintained as hemizygous on the BL6 background. Animals were group housed on a 12 h light/dark cycle with Nestlet enrichment and killed at ages 18 M, 12 M, 6 M, 4 M, 2 M, 1 M as noted in the text.

**Mouse tissue fixation.** Mice were deeply anesthetized with isoflurane (Isoflurane, USP, Piramal Healthcare, Andhra Pradesh, India) and underwent transcardial perfusion with ice-cold 1 $\times$  PBS (10 $\times$  stock, Gibco, #70011-044) followed by ice-cold fixative made of 4% paraformaldehyde (32% stock, Electron Microscopy Sciences (EMS), Hatfield, PA, #15714) and 1% glutaraldehyde (10% stock, EMS #16110) in 1 $\times$  PBS. Brains were removed from the skull and postfixed in the same fixative for 3 days shaking at 4 $^{\circ}$ C.

**Intact mouse brain SWITCH processing.** After washing in 1 $\times$  PBS, brains incubated in inactivation solution of 1% acrylamide (40% stock, Biorad #161-0140), 1 M glycine (Sigma-Aldrich, St. Louis, MO, #G7126) in 1 $\times$  PBS. After washing in 1 $\times$  PBS, brains were put into clearing solution of 200 mM sodium dodecyl sulfate (SDS) (Sigma-Aldrich, #L3771), 20 mM lithium hydroxide monohydrate (Sigma, #254274), 40 mM boric acid (Sigma-Aldrich, #7901), pH 8.5–9.0 and left shaking at 55 $^{\circ}$ C for 4 weeks until white matter tracts were translucent to the eye in SDS. Brains were washed in 1 $\times$  PBS or Weak Binding Solution (WBS) for up to 1 week and immunolabeled with the SWITCH protocol for labeling intact mouse brain (Supplementary Methods).

**Mouse brain section processing.** Where sections were analyzed, brains were sliced to 100  $\mu$ m on a vibratome (Leica VT100S) and stored at 4 $^{\circ}$ C in 1 $\times$  PBS + 0.02% sodium azide (Sigma-Aldrich, #S2002). For SWITCH labeling, individual sections were incubated in clearing solution shaking at 55 $^{\circ}$ C for 2 h and were washed in 1 $\times$  PBS. Sections were immunolabeled with the SWITCH protocol for labeling mouse brain sections (Supplementary Methods), and antigens targeted are noted in the text.

**Intact human tissue SWITCH processing.** Human tissue blocks were deparaffinized by sequential immersion in xylene, ethanol, and water (details in Human SWITCH protocol). Then, blocks were incubated in 1% GA in 1 $\times$  PBS for 10 days at 4 $^{\circ}$ C. Brains were incubated in clearing solution shaking at 55 $^{\circ}$ C until the tissue appeared translucent (4–8 weeks). Following clearing, tissue was labeled using the SWITCH protocol for labeling human autopsy specimens (Supplementary Methods).

**Human specimen tissue section processing.** Tissue from the Netherlands Brain Bank (Supplementary Movie 3): Formalin-fixed paraffin-embedded human post-mortem tissue blocks were sectioned at 5- $\mu$ m thickness, dried at room temperature for 24 h and heated at 80 $^{\circ}$ C for 24 h before IHC processing. Deparaffinization, antigen retrieval, and subsequent staining were performed with Boston Medical Center Pathology Department's Ventana Benchmark Ultra automated IHC instrument using commercially available primary antibodies specific for A $\beta$  (mouse anti-human beta-amyloid [6F/3D] monoclonal antibody, 1:50, Dako, Glostrup, Denmark), visualized by HRP-conjugated secondary antibody with diaminobenzidine (DAB) chromogen.

Tissue from the Religious Orders Study (Supplementary Fig. 2): Formalin-fixed tissue was embedded in 2% agarose gel and sectioned at 40- $\mu$ m thickness into 1 $\times$  PBS. Slices were blocked with 2% bovine serum albumin in 1 $\times$  PBS with 0.1% triton x-100 and then incubated in CST-D54D2 anti-A $\beta$  primary. After washing, sections were incubated in AlexaFluor-conjugated secondary. After a final wash, including DAPI for nuclear identification, sections were mounted for imaging in Fluoromount G.

**Antibodies and dyes.** The primary antibodies used are shown in Table 3. Hoechst 33258 (Sigma #14530) and DAPI (ThermoFisher Scientific, #D1306) were used for nuclear labeling. All secondary antibodies were Pre-adsorbed F(ab)2' AlexaFluor-conjugated from AbCam.

**Intact brain image acquisition.** Intact brain images were acquired on a custom SPIM microscope built by H.C. During imaging, samples were illuminated with a sheet of light generated by scanning a focused beam from a light source (SOLE –6 with 488, 561, 647 nm, Omicron) through a low NA objective (Macro 4X/0.28 NA, Olympus) with a galvo-scanner (6215 H, Cambridge Technology). Collection of emitted light on the microscope occurs through a long working distance high NA objective (10 $\times$ /0.6 NA WD 8 mm CLARITY, Olympus). The microscope is outfitted with four sCMOS cameras (Orca Flash4.0 V2, Hamamatsu) for simultaneous multichannel signal recording. During acquisition, the samples were illuminated simultaneously from dual illumination arms (one on each side) to minimize the shading effects of light-scattering elements in the brain. Dynamic confocal mode of detection is implemented by synchronizing the scanning speed of the illumination beam with the read-out speed of the rolling shutter mode of sCMOS camera, which improves the signal to background ratio by filtering out background signal from out-of-focal regions. Sample is mounted on a motorized stage with x, y, z translation and theta rotation (two of M-112.2DG, M-111K028, M-116.DG, Physik Instrumente) for mosaic imaging. Z-stack imaging by sample scanning alone is slow due to communication overhead between the host computer and the stage controller. We achieved high-speed volume imaging by scanning the light sheet along the depth direction with a galvo-scanner and synchronizing the position of the light sheet with the detection objective's focal plane by moving the detection objective with a piezo actuator (P-628.1CL, Physik Instrumente). To maintain light sheet position on the focal plane of the objective across the entire sample volume, we implemented an image-based autofocus algorithm<sup>66</sup>. The laser settings are determined such that ~5% of the images are saturated to its maximum gray level for high signal to background ratio. The sample chamber is filled with the refractive index-matching solution (RIMS)<sup>67</sup>. Depending on the refractive index of the medium, the beam waist position of the illumination light sheet shifts along the illumination beam direction. Each illumination objective is mounted on the piezo actuator (P-628.1CL, Physik Instrumente) to allow the beam waist position to be adjusted to the center of the detection objective. Sample chamber is specially designed to allow for free motion of the detection objective while preventing leakage of the immersion medium.

**Intact brain image processing.** Each tile is first corrected for the nonuniform illumination pattern using a modified algorithm from Smith et al.<sup>68</sup>. Multiple stacks of acquired images are stitched with Terastitcher<sup>69</sup>. Each tile has 15% overlapping area with the neighboring tiles for calculating stitching parameters. The voxel size of raw data is 0.58  $\times$  0.58  $\times$  5.0  $\mu$ m. The raw data set is first down-sampled four times in X and Y dimension and then stitched to ease the computation burden in the downstream analysis. The stitched data set is analyzed with Imaris software (Bitplane).

**Section image acquisition.** For section and human tissue imaging, tissue was mounted onto microscope slides (VWR VistaVision, VWR International, LLC, Radnor, PA, USA) with either Fluoromount G Mounting Medium (Electron Microscopy Sciences, Hatfield, PA, USA) or RIMS solution<sup>67</sup>.

Confocal slice images were acquired on a Zeiss LSM Inverted 710 microscope using Zen 2012 software (Carl Zeiss Microscopy, Jena, Germany). Images with cellular resolution were taken using a C-apochromat 40X, water immersion objective, NA 1.20. Section overview images used a Plan-apochromat 5X, air objective, NA 0.16. Pinhole, optical sectioning, and laser settings were determined for each experiment, and kept consistent for all images within an experiment or that were included within one analysis.

**Human brain image acquisition.** Human brain images were acquired on a Leica TCS SP8 Confocal Microscope using LASAF software (Leica Microsystems, Wetzlar, Germany). Images were taken using a  $\times$ 25 1.0NA CLARITY optimized objective with 6 mm working distance. The pinhole, optical sectioning, and resolution and laser settings were empirically determined for one brain, and kept constant for imaging subsequent samples.

**3D image quantification.** Images were analyzed using Imaris (Bitplane, Zurich, Switzerland). All quantification steps were performed on raw images by blinded investigators. For intact tissue analyses (Fig. 1), each brain file was segmented by hand using white matter tract and regional guidelines from the Allen Brain Atlas (Allen Mouse Brain Atlas, Coronal) to delineate boundaries for each major brain region (Supplementary Movie 4). After segmentation, a spots object was created on a 12-month brain. The parameters were fixed over the entire brain, and spots were separated into the bounded brain regions using the Spots into Surfaces tool in Imaris Xtensions. A spots object was created on each brain, and these objects were similarly split into brain regions using the Xtension. The data were exported to CSV and analyzed GraphPad Prism 7.0a for Mac.

**Table 3 Primary antibodies used in this study**

Target	Host	Company	Product #	Dilution
A $\beta$ [D54D2]	Rabbit	Cell Signaling Technologies	8243	1:100–1000
Myelin Basic Protein <sup>a</sup> SMI-99	Mouse	BioLegend	808401	1:50–500
Myelin Basic Protein <sup>a</sup> SMI-94	Mouse	BioLegend	836502	1:50–500
$\beta$ -amyloid [6 F/3D]	Mouse	Dako	M087201–2	1:50

<sup>a</sup>These antibodies were used concurrently as per the manufacturer's recommendation

**Table 4 Primer sequences (5'–3') for in situ probe preparation**

Gene	Forward primer	Reverse primer
hAPP	GAGACACCTGGGGATGAGAA	TAATACGACTCACTATAGGGACAGAGTCAGCCCCAAAAGA

**2D image quantification.** For 2D analyses, images were imported into FIJI<sup>70</sup> as LSM files. Numerical data were saved in a spreadsheet and exported to GraphPad Prism 7.0a for Mac for statistical analyses. For ISH-IF analyses, blinded observers outlined three regions of interest (ROI) within each brain area looking only at the image containing APP-ISH information. The same regions were overlaid on the amyloid-IF image for quantification of the A $\beta$  signal. For human amyloid analyses (Supplementary Fig. 2), two blinded observers counted plaques within images using the Multi-point tool. Then the segmentation was overlaid on the A $\beta$  channel as a selection, within which a threshold was applied to the images. Finally, a Analyze Particles tool was used to count individual deposits. In all figures with 2D images, quantification was performed on raw, unaltered image data. For visibility at print resolution, representative images in Fig. 2 have had the brightness and contrast adjusted. All contrast and brightness adjustments were made identically across all images within a figure. Raw images are available upon request.

#### Representative images and supplementary movies from intact brain data.

Representative images from the intact brain data sets are either 2D images of the 3D-rendered data set or digitally sectioned at 5–100  $\mu$ m in Imaris using the Orthoslicer tool. Supplementary Movies are created using the Key Frame Animation tool in Imaris. The brightness of the images has been individually adjusted for each brain to enhance 2D/3D viewing of specific objects. Because of these alterations, no direct comparisons of labeling intensity should be made between images.

**In situ hybridization probe design.** RNA antisense probes were generated by PCR-amplifying human cDNA with human-specific APP primers with a T7 RNA polymerase recognition sequence (TAATACGACTCACTATAGGG) fused to the reverse primer (Table 4). The resulting PCR product was gel extracted and in vitro transcribed using a DIG-RNA labeling kit (Roche).

**Immuno-in situ hybridization (Immuno-ISH).** Mice were anesthetized by isoflurane in an open system and perfused with RNase-free PBS followed by RNase-free 4% formaldehyde. Brains were dissected, drop fixed in RNase-free 4% formaldehyde for 12 h, equilibrated in 30% sucrose-PBS, and frozen in O.C.T. (Tissue-Tek). Cryosections (10  $\mu$ m) were incubated with a DIG-labeled RNA antisense probe (1:1000 in hybridization buffer) overnight at 65 °C, washed in 1 $\times$  SSC/50% formamide/0.1% Tween-20 3 $\times$  30 min at 65 °C followed by 1 $\times$  MABT for 30 min at room temperature. Sections were blocked with 20% heat-inactivated sheep serum/2% blocking reagent (Roche)/1 $\times$  MABT for 1 h and then incubated with mouse anti-DIG antibody (Roche; 1:2000) and rabbit anti-amyloid  $\beta$  (Cell Signaling; 1:500) diluted in blocking solution overnight. Sections were washed with 1 $\times$  MABT 2 $\times$  20 min, incubated with donkey anti-rabbit Alexa-488 (Invitrogen; 1:1000) diluted in blocking solution for 1 h, and washed with 1 $\times$  MABT 5 $\times$  20 min. Sections were then prestained with 100 mM NaCl/50 mM MgCl<sub>2</sub>/100 mM Tris pH 9.5/0.1% Tween-20 2 $\times$  10 min, followed by staining with NBT/BCIP (Roche; 4.5  $\mu$ l/ml and 3.5  $\mu$ l/ml, respectively, in prestaining buffer) for 2 h. Sections were washed with 1 $\times$  PBS 3 $\times$  15 min, incubated in xylene 3 $\times$  5 min, and mounted with VectaMount (Vector Laboratories).

**Slice electrophysiology.** Acute brain slices were prepared from male and female 5XFAD mice and WT littermate controls, aged 2–2.5-months old. The experimenter was blinded to the group of animal. The mice were anesthetized with isoflurane and decapitated. After decapitation, the brains were rapidly removed, and a cut was made to remove the cerebellum. The brain was mounted anterior-side up. Coronal brain slices (250- $\mu$ m thick) were prepared in ice-cold dissection buffer bubbled with 95% O<sub>2</sub>–5% CO<sub>2</sub> containing (in mM) 211 sucrose, 3.3 KCl, 1.3

NaH<sub>2</sub>PO<sub>4</sub>, 0.5 CaCl<sub>2</sub>, 10 MgCl<sub>2</sub>, 26 NaHCO<sub>3</sub> and 11 D-glucose using a Leica VT1000S vibratome (Leica). Slices were recovered in a holding chamber with 95% O<sub>2</sub>/5% CO<sub>2</sub>-saturated artificial cerebrospinal fluid (ACSF) consisting of (in mM) 124 NaCl, 3.3 KCl, 1.3 NaH<sub>2</sub>PO<sub>4</sub>, 2.5 CaCl<sub>2</sub>, 1.5 MgCl<sub>2</sub>, 26 NaHCO<sub>3</sub>, and 11 D-glucose for 1 h at 32 °C and then stored at room temperature. Individual slices for recording were then transferred to a submerged recording chamber and perfused with ACSF at a constant rate of 2–2.5 ml/min at room temperature. Cells were visualized using infrared differential interference contrast (IR-DIC) imaging on an Olympus BX-50WI microscope. Action potentials (APs) in whole-cell current patch clamp from mammillary body were acquired on an EPC10 amplifier (HEKA Elektronik) with Patchmaster software. APs were elicited by current clamp of current steps from 0 pA to +100 pA at 10 pA increments for 800 ms. Signals were filtered at 2 KHz and stored on a personal computer (PC). A borosilicate glass electrode (resistance of 6–7 M $\Omega$ ) with pipette solution containing (in mM) 130 K gluconate; 20 KCl; 10 HEPES; 0.2 EGTA, 4 MgATP, 0.3 Na<sub>2</sub>GTP, 10 disodium phosphocreatine was used. APs and resting membrane potentials (RMP) were analyzed using Patchmaster software (HEKA Elektronik). Statistics were calculated in Prism as described below and in the text. The data are represented as outlined in the text and figure legends.

**DREADD experiments.** 5XFAD mice were anaesthetized with isoflurane in the stereotaxic frame for the entire surgery, and their body temperature was maintained with a heating pad. In order to inhibit neuronal activity in the mammillary body (MB), 200 nl of adeno-associated virus carrying inhibitory DREADD, hM4Di and mCherry (pAAV-CamKII $\alpha$ -hM4Di-mCherry, Addgene, catalog #50477-AAV8) were injected into the MB (From bregma: A|P: –2.0 mm, M|L: 0.0 mm, D|V: –5.6 mm). Injections were performed at a rate of 50 nl per min. The needle was allowed to sit in the target location for 3 min prior to the start of viral infusion and for 5 min after injection was completed. 5XFAD mice injected with AAV-CamKII $\alpha$ -EGFP (AAV-CamKII $\alpha$ -GFP, University of North Carolina Vector Core) in the MB were used as control group. We allowed for 3 weeks of post-operative recovery and time for expression of viral vectors. Mice were then given i.p. injections of clozapine-n-oxide (CNO, Tocris, catalog #4936/50) at 3 mg/kg body weight, daily for 5 weeks. CNO was dissolved in saline with a working solution at 0.5 mg/ml. To control the CNO effect, both control and mice with expression of inhibitory DREADD were injected with CNO in the experiment.

**Statistics and reproducibility.** All statistics were performed in MatLab or GraphPad Prism. Individual statistical tests are indicated in the text and/or figure legends for the appropriate experiments. Data sets were checked for normality and statistics were run depending on the appropriateness of parametric or nonparametric tests for the normality of the data. Graphs were created in the respective analytical software packages and exported as .TIFF for inclusion in the document. Sample sizes reported in the text and figures represent numbers of independent samples used in the analysis (e.g., animal numbers, unique human patients, etc), unless otherwise noted in the text.

**Reporting summary.** Further information on research design is available in the Nature Research Reporting Summary linked to this article.

#### Data availability

All data reported in this paper including raw image files are available upon request. Images are stored as.lsm,.czi,.tif or.lei files. Imaris files are stored as.ims. The data can be requested from the Tsai Laboratory by emailing tsaisst@mit.edu or contacting one of the corresponding authors. Resources that may help enable general users to establish the methodology are freely available online (<http://www.chunglabresources.org>).

Received: 5 June 2019; Accepted: 4 September 2019;

Published online: 04 October 2019

## References

- Hurd, M. D., Martorell, P., Delavande, A., Mullen, K. J. & Langa, K. M. Monetary costs of dementia in the United States. *N. Engl. J. Med.* **368**, 1326–1334 (2013).
- Hardy, J. & Higgins, G. Alzheimer's disease: the amyloid cascade hypothesis. *Science* **256**, 184–185 (1992).
- Musiek, E. S. & Holtzman, D. M. Three dimensions of the amyloid hypothesis: time, space and 'wingmen'. *Nat. Neurosci.* **18**, 800 (2015).
- Jack, C. R. et al. NIA-AA research framework: toward a biological definition of Alzheimer's disease. *Alzheimer's. Dement* **14**, 535–562 (2018).
- Mutations | AlzForum. Available at: <http://www.alzforum.org/mutations/> (Accessed October 20, 2016).
- Kimura, R. & Ohno, M. Impairments in remote memory stabilization precede hippocampal synaptic and cognitive failures in 5XFAD Alzheimer mouse model. *Neurobiol. Dis.* **33**, 229–235 (2009).
- Palop, J. J. et al. Aberrant excitatory neuronal activity and compensatory remodeling of inhibitory hippocampal circuits in mouse models of Alzheimer's disease. *Neuron* **55**, 697–711 (2007).
- Huijbers, W. et al. Amyloid-beta deposition in mild cognitive impairment is associated with increased hippocampal activity, atrophy and clinical progression. *Brain* **138**, 1023–1035 (2015).
- Hong, S. et al. Complement and microglia mediate early synapse loss in Alzheimer mouse models. *Science* **337**, 1–9 (2016).
- Wei, W. et al. Amyloid beta from axons and dendrites reduces local spine number and plasticity. *Nat. Neurosci.* **13**, 190–196 (2010).
- Scheuner, D. et al. Secreted amyloid beta-protein similar to that in the senile plaques of Alzheimer's disease is increased in vivo by the presenilin 1 and 2 and APP mutations linked to familial Alzheimer's disease. *Nat. Med.* **2**, 864–870 (1996).
- Thal, D. R., Rüb, U., Orantes, M. & Braak, H. Phases of A beta-deposition in the human brain and its relevance for the development of AD. *Neurology* **58**, 1791–1800 (2002).
- Mormino, E. C. et al. Synergistic effect of  $\beta$ -amyloid and neurodegeneration on cognitive decline in clinically normal individuals. *JAMA Neurol.* **71**, 1379–1385 (2014).
- Jack, C. R. et al. Brain beta-amyloid measures and magnetic resonance imaging atrophy both predict time-to-progression from mild cognitive impairment to Alzheimer's disease. *Brain* **133**, 3336–3348 (2010).
- Buckner, R. L., Andrews-Hanna, J. R. & Schacter, D. L. The brain's default network: anatomy, function, and relevance to disease. *Ann. N. Y. Acad. Sci.* **1124**, 1–38 (2008).
- Villemagne, V. L. et al. Amyloid imaging with 18F-florbetaben in Alzheimer disease and other dementias. *J. Nucl. Med.* **52**, 1210–1217 (2011).
- Klunk, W. E. et al. Imaging brain amyloid in Alzheimer's disease with Pittsburgh compound-B. *Ann. Neurol.* **55**, 306–319 (2004).
- Villemagne, V. L. et al. Longitudinal assessment of A $\beta$  and cognition in aging and Alzheimer disease. *Ann. Neurol.* **69**, 181–192 (2011).
- Grothe, M. J. et al. In vivo staging of regional amyloid deposition. *Neurology* **89**, 2031–2038 (2017).
- Akhtar, R. S. et al. Regional brain amyloid- $\beta$  accumulation associates with domain-specific cognitive performance in Parkinson disease without dementia. *PLoS ONE* **12**, e0177924 (2017).
- Jack, C. R. et al. Rates of beta-amyloid accumulation are independent of hippocampal neurodegeneration. *Neurology* **82**, 1605–1612 (2014).
- Greicius, M. D., Srivastava, G., Reiss, A. L. & Menon, V. Default-mode network activity distinguishes Alzheimer's disease from healthy aging: evidence from functional MRI. *Proc. Natl Acad. Sci. USA* **101**, 4637–4642 (2004).
- Fletcher, E. et al. Beta-amyloid, hippocampal atrophy and their relation to longitudinal brain change in cognitively normal individuals. *Neurobiol. Aging* **40**, 173–180 (2016).
- Fletcher, E., Carmichael, O., Pasternak, O., Maier-Hein, K. H. & DeCarli, C. Early brain loss in circuits affected by Alzheimer's disease is predicted by fornix microstructure but may be independent of gray matter. *Front. Aging Neurosci.* **6**, 106 (2014).
- Bakker, A., Albert, M. S., Krauss, G., Speck, C. L. & Gallagher, M. Response of the medial temporal lobe network in amnesic mild cognitive impairment to therapeutic intervention assessed by fMRI and memory task performance. *NeuroImage Clin.* **7**, 688–698 (2015).
- Reitz, C. & Mayeux, R. Alzheimer disease: epidemiology, diagnostic criteria, risk factors and biomarkers. *Biochem. Pharmacol.* **88**, 640–651 (2014).
- De Strooper, B. & Karran, E. The cellular phase of Alzheimer's disease. *Cell* **164**, 603–615 (2016).
- Oakley, H. et al. Intraneuronal  $\beta$ -amyloid aggregates, neurodegeneration, and neuron loss in transgenic mice with five familial Alzheimer's disease mutations: potential factors in amyloid plaque formation. *J. Neurosci.* **26**, 10129–10140 (2006).
- Murray, E. et al. Simple, scalable proteomic imaging for high-dimensional profiling of intact systems. *Cell* **163**, 1500–1514 (2015).
- Barnes, A. The specificity of pH and ionic strength effects on the kinetics of the Rh (D)-anti-Rh (D) system. *J. Immunol.* **96**, 854–864 (1966).
- Eimer, W. A. & Vassar, R. Neuron loss in the 5XFAD mouse model of Alzheimer's disease correlates with intraneuronal A $\beta$ 42 accumulation and Caspase-3 activation. *Mol. Neurodegener.* **8**, 2 (2013).
- Richardson, D. S. & Lichtman, J. W. Clarifying tissue clearing. *Cell* **162**, 246–257 (2015).
- Jost, B. C. & Grossberg, G. T. The evolution of psychiatric symptoms in Alzheimer's disease: a natural history study. *J. Am. Geriatr. Soc.* **44**, 1078–1081 (1996).
- Stafford, J. M. et al. Large-scale topology and the default mode network in the mouse connectome. *Proc. Natl Acad. Sci. USA* **111**, 18745–18750 (2014).
- Hedden, T. et al. Disruption of functional connectivity in clinically normal older adults harboring amyloid burden. *J. Neurosci.* **29**, 12686–12694 (2009).
- Sperling, R., LaViolette, P. & O'Keefe, K. Amyloid deposition is associated with impaired default network function in older persons without dementia. *Neuron* **63**, 178–188 (2009).
- Aggleton, J. P., Pralus, A., Nelson, A. J. D. & Hornberger, M. Thalamic pathology and memory loss in early Alzheimer's disease: moving the focus from the medial temporal lobe to Papez circuit. *Brain* aww083. <https://doi.org/10.1093/brain/aww083> (2016).
- Siskova, Z. et al. Dendritic structural degeneration is functionally linked to cellular hyperexcitability in a mouse model of Alzheimer's disease. *Neuron* **84**, 1023–1033 (2014).
- Vossel, K. A. et al. Seizures and epileptiform activity in the early stages of Alzheimer disease. *JAMA Neurol.* **70**, 1158–1166 (2013).
- Tsviliv, D. et al. A disproportionate role for the fornix and mammillary bodies in recall versus recognition memory. *Nat. Neurosci.* **11**, 834–842 (2008).
- Roy, D. S. et al. Distinct neural circuits for the formation and retrieval of episodic memories. *Cell* **170**, 1000–1012.e19 (2017).
- Dillingham, C. M., Frizzati, A., Nelson, A. J. D. & Vann, S. D. How do mammillary body inputs contribute to anterior thalamic function? *Neurosci. Biobehav. Rev.* **54**, 108–119 (2015).
- Cirrito, J. R. et al. Synaptic activity regulates interstitial fluid amyloid-beta levels in vivo. *Neuron* **48**, 913–922 (2005).
- Bero, A. W. et al. Neuronal activity regulates the regional vulnerability to amyloid- $\beta$  deposition. *Nat. Neurosci.* **14**, 750–756 (2011).
- Yamamoto, K. et al. Chronic optogenetic activation augments A $\beta$  pathology in a mouse model of Alzheimer disease. *Cell Rep.* **11**, 859–865 (2015).
- Yuan, P. & Grutzendler, J. Attenuation of -amyloid deposition and neurotoxicity by chemogenetic modulation of neural activity. *J. Neurosci.* **36**, 632–641 (2016).
- Zhu, H. et al. Chemogenetic inactivation of ventral hippocampal glutamatergic neurons disrupts consolidation of contextual fear memory. *Neuropsychopharmacology* **39**, 1880–1892 (2014).
- Copenhaver, B. R. et al. The fornix and mammillary bodies in older adults with Alzheimer's disease, mild cognitive impairment, and cognitive complaints: a volumetric MRI study. *Psychiatry Res.: Neuroimaging* **147**, 93–103 (2006).
- Hornberger, M. et al. In vivo and post-mortem memory circuit integrity in frontotemporal dementia and Alzheimer's disease. *Brain* **135**, 3015–3025 (2012).
- Nestor, P. J., Fryer, T. D., Smielewski, P. & Hodges, J. R. Limbic hypometabolism in Alzheimer's disease and mild cognitive impairment. *Ann. Neurol.* **54**, 343–351 (2003).
- Braak, H. & Braak, E. Neuropathological staging of Alzheimer-related changes. *Acta Neuropathol.* **82**, 239–259 (1991).
- Allen, G. V. & Hopkins, D. A. Mammillary body in the rat: topography and synaptology of projections from the subicular complex, prefrontal cortex, and midbrain tegmentum. *J. Comp. Neurol.* **286**, 311–336 (1989).
- Terry, R. D. et al. Physical basis of cognitive alterations in Alzheimer's disease: synapse loss is the major correlate of cognitive impairment. *Ann. Neurol.* **30**, 572–580 (1991).
- DeKosky, S. T. & Scheff, S. W. Synapse loss in frontal cortex biopsies in Alzheimer's disease: Correlation with cognitive severity. *Ann. Neurol.* **27**, 457–464 (1990).
- Scheff, S. W. & Price, D. A. Synapse loss in the temporal lobe in Alzheimer's disease. *Ann. Neurol.* **33**, 190–199 (1993).

56. Hyman, B. T., Van Hoesen, G. W., Damasio, A. R. & Barnes, C. L. Alzheimer's disease: cell-specific pathology isolates the hippocampal formation. *Science* **225**, 1168–1170 (1984).
57. Whitehouse, P. J., Price, D. L., Clark, A. W., Coyle, J. T. & DeLong, M. R. Alzheimer disease: evidence for selective loss of cholinergic neurons in the nucleus basalis. *Ann. Neurol.* **10**, 122–126 (1981).
58. Li, W. et al. Aberrant functional connectivity in Papez circuit correlates with memory performance in cognitively intact middle-aged APOE4 carriers. *Cortex* **57**, 167–176 (2014).
59. Rönnbäck, A. et al. Amyloid neuropathology in the single Arctic APP transgenic model affects interconnected brain regions. *Neurobiol. Aging*. <https://doi.org/10.1016/j.neurobiolaging.2011.07.012> (2012).
60. Dean 3rd, D. et al. Association of amyloid pathology with myelin alteration in preclinical Alzheimer disease. *JAMA Neurol.* **74**, 41–49 (2017).
61. Verret, L. et al. Inhibitory interneuron deficit links altered network activity and cognitive dysfunction in alzheimer model. *Cell* **149**, 708–721 (2012).
62. Ye, L. et al. Progression of seed-induced abeta deposition within the limbic connectome. *Brain Pathol.* **25**, 743–752 (2015).
63. Roy, D. S. et al. Memory retrieval by activating engrgram cells in mouse models of early Alzheimer's disease. *Nature*. <https://doi.org/10.1038/nature17172> (2016).
64. Iaccarino, H. F. et al. Gamma frequency entrainment attenuates amyloid load and modifies microglia. *Nature* **540**, 230–235 (2016).
65. Donohue, M. C. et al. Association between elevated brain amyloid and subsequent cognitive decline among cognitively normal persons. *JAMA* **317**, 2305 (2017).
66. Tomer, R., Ye, L., Hsueh, B. & Deisseroth, K. Advanced CLARITY for rapid and high-resolution imaging of intact tissues. *Nat. Protoc.* **9**, 1682–1697 (2014).
67. Yang, B. et al. Single-cell phenotyping within transparent intact tissue through whole-body clearing. *Cell* **158**, 945–958 (2014).
68. Smith, K. et al. CIDRE: an illumination-correction method for optical microscopy. *Nat. Methods* **12**, 404 (2015).
69. Bria, A. & Iannello, G. TeraStitcher—a tool for fast automatic 3D-stitching of teravoxel-sized microscopy images. *BMC Bioinforma.* **13**, 316 (2012).
70. Schindelin, J. et al. Fiji: an open-source platform for biological-image analysis. *Nat. Methods* **9**, 676–682 (2012).

## Acknowledgements

The authors would like to acknowledge Michiel Kooreman at the Netherlands Brain Bank for help procuring the PPFE human tissue and Teresa Lima for her expert advice in preparing the human PPFE brain tissue for the optimized CLARITY protocol. We would also like to thank Nina Dedic for her advice and helpful comments on the project and paper. In addition, we would like to acknowledge Naveed Bakh, Sung-Yon Kim, and Kamilla Tekiela for helping lay the groundwork for the experiments presented in this

work. This work was funded by Ludwig Foundation, NIH grant RF1AG047661 and JPB Foundation Funding (PIIF and PNDRF) to L.-H.T. and by the Norman B. Leventhal and Barbara Weedon fellowships to R.G.C. In addition, K.C. was supported by Burroughs Wellcome Fund Career Awards at the Scientific Interface, the Searle Scholars Program, Packard award in Science and Engineering, NARSAD Young Investigator Award, JPB Foundation (PIIF and PNDRF), NCSOFT Cultural Foundation, and NIH (1-U01-NS090473-01, P30AG10161, and RF1AG15819).

## Author contributions

R.G.C., W.-C.H., K.C., L.-H.T., and I.D. conceived the work and wrote the paper. R.G.C., W.-C.H., H.C., J.W., and L.A.W. designed the experiments. R.G.C., W.-C.H., H.C., J.W., L.A.W., C.G.Y., F.A., and S.M.B. performed experiments and analyzed data. D.A.B. and I.D. helped analyze data and contributed to the preparation of the paper. W.-C.H., J.Z.Y., and H.C. contributed to the preparation of the paper. H.C. built the custom microscope.

## Competing interests

The authors declare no competing interests.

## Additional information

**Supplementary information** is available for this paper at <https://doi.org/10.1038/s42003-019-0599-8>.

**Correspondence** and requests for materials should be addressed to I.D., K.C. or L.-H.T.

**Reprints and permission information** is available at <http://www.nature.com/reprints>

**Publisher's note** Springer Nature remains neutral with regard to jurisdictional claims in published maps and institutional affiliations.



**Open Access** This article is licensed under a Creative Commons Attribution 4.0 International License, which permits use, sharing, adaptation, distribution and reproduction in any medium or format, as long as you give appropriate credit to the original author(s) and the source, provide a link to the Creative Commons license, and indicate if changes were made. The images or other third party material in this article are included in the article's Creative Commons license, unless indicated otherwise in a credit line to the material. If material is not included in the article's Creative Commons license and your intended use is not permitted by statutory regulation or exceeds the permitted use, you will need to obtain permission directly from the copyright holder. To view a copy of this license, visit <http://creativecommons.org/licenses/by/4.0/>.

© The Author(s) 2019